A novel topographic parameterization scheme indicates that martian gullies display the signature of liquid water

Susan J. Conway, Matthew Balme

A novel topographic parameterization scheme indicates that martian gullies display the signature of liquid water

Susan J. Conway[1,2*], and Matthew R. Balme[1]

[1]*Department of Physical Sciences, Open University, Milton Keynes, MK7 6AA UK.*

[2]*Now at : Laboratoire de Planétologie et Géodynamique, UMR 6112, CNRS, Université de Nantes, 2 chemin de la Houssinière, BP 92205, 44322 Nantes Cedex 3, France.*

**Correspondence to: susan.conway@univ-nantes.fr.*

Keywords: Mars; Martian Gullies; Planetary Geomorphology; Geomorphometry

Highlights:

- We present new terrain analyses from high-resolution DEMs of martian gullies
- We find that liquid water was involved in the formation of martian gullies
- Dry processes do not explain gullies topographic signatures
- Process-level interpretation from 2D images can be unreliable
- Statistical analysis of 3D data provides a better way to determine process

Abstract

Martian gullies resemble gullies carved by water on Earth, yet are thought to have formed in an extremely cold (<-50°C) and dry (humidity < 100 precipitable micrometers) surface environment (c.f. Mellon et al., 2004). Despite more than a decade of observations, no consensus has emerged as to whether liquid water is required to form martian gullies, with some recent studies favoring dry CO_2-driven processes. That this argument persists demonstrates the limitations of morphological interpretations made from 2D images, especially when similar-looking landforms can form by very different processes. To overcome this we have devised a parametrization scheme, based on statistical discriminant analysis and hydrological terrain analysis of meter-scale digital topography data, which can distinguish between dry and wet surface processes acting on a landscape. Applying this approach to new meter-scale topographic datasets of Earth, the Moon and Mars, we demonstrate that martian gullied slopes are dissimilar to dry, gullied slopes on Earth and the Moon, but are similar to both terrestrial debris flows and fluvial gullies. We conclude that liquid water was integral to the process by which martian gullies formed. Finally, our work shows that quantitative 3D analyses of landscape have great potential as a tool in planetary science, enabling remote assessment of processes acting on planetary surfaces.

1. 0 Introduction

Gullies on Mars (Malin and Edgett, 2000) are widespread: they are concentrated in the mid-latitudes and can be found on steep slopes polewards of about 30° (Dickson et al., 2007). Global and hemispheric studies have revealed that mid-latitude gullies are located on slopes oriented towards the pole (Balme et al., 2006; Bridges and Lackner, 2006; Dickson et al., 2007; Harrison et al., 2015; Heldmann et al., 2007; Heldmann and Mellon, 2004; Kneissl et al., 2010; Marquez et al., 2005) while higher latitude examples have little, or no preferred orientation. The distribution and orientation of gullies are consistent with their formation at high obliquity, when pole-facing slopes receive maximum summer insolation. Together, this evidence led to the conclusion that gullies formed as water-rich debris flows (Costard et al., 2002).

However, increased insolation can also trigger dry mass wasting or destabilization of solid CO_2. Narrow channels observed on the Moon (Bart, 2007; Senthil Kumar et al., 2013; Xiao et al., 2013) and on the asteroid Vesta (Krohn et al., 2014; Scully et al., 2015) have been identified as analogues to martian gullies by some authors, yet these exist on airless bodies where erosion by traditional low-viscosity fluids is unlikely and whose surfaces are almost certainly completely dry. Hence, dry mass-wasting has been considered a potential formation mechanism for martian gullies. Some of the recent modifications observed in martian gullies, including new deposits and channel formation, have been found to occur at the time of year when CO_2 frost is subliming (Dundas et al., 2015, 2012, 2010; Raack et al., 2015; Vincendon, 2015). Therefore mechanisms involving gas release triggering granular flow (Cedillo-Flores et al., 2011; Pilorget and Forget, 2016), have been suggested for gully-formation. Theoretical modelling (Cedillo-Flores et al., 2011) predicts that sand-sized or smaller grains can be mobilized by CO_2 gas-sublimation under martian conditions but, unless there is a confining "lid" (Pilorget and Forget, 2016) on the flow, it rapidly converts from a gas-supported to a

simple granular flow. Hence, we consider the visually-similar, gully-like granular flows observed on the Moon as suitable analogues for this process. We also consider mass-wasting deposits on Earth, in which water likely played a very minor role, as possible analogues for this process.

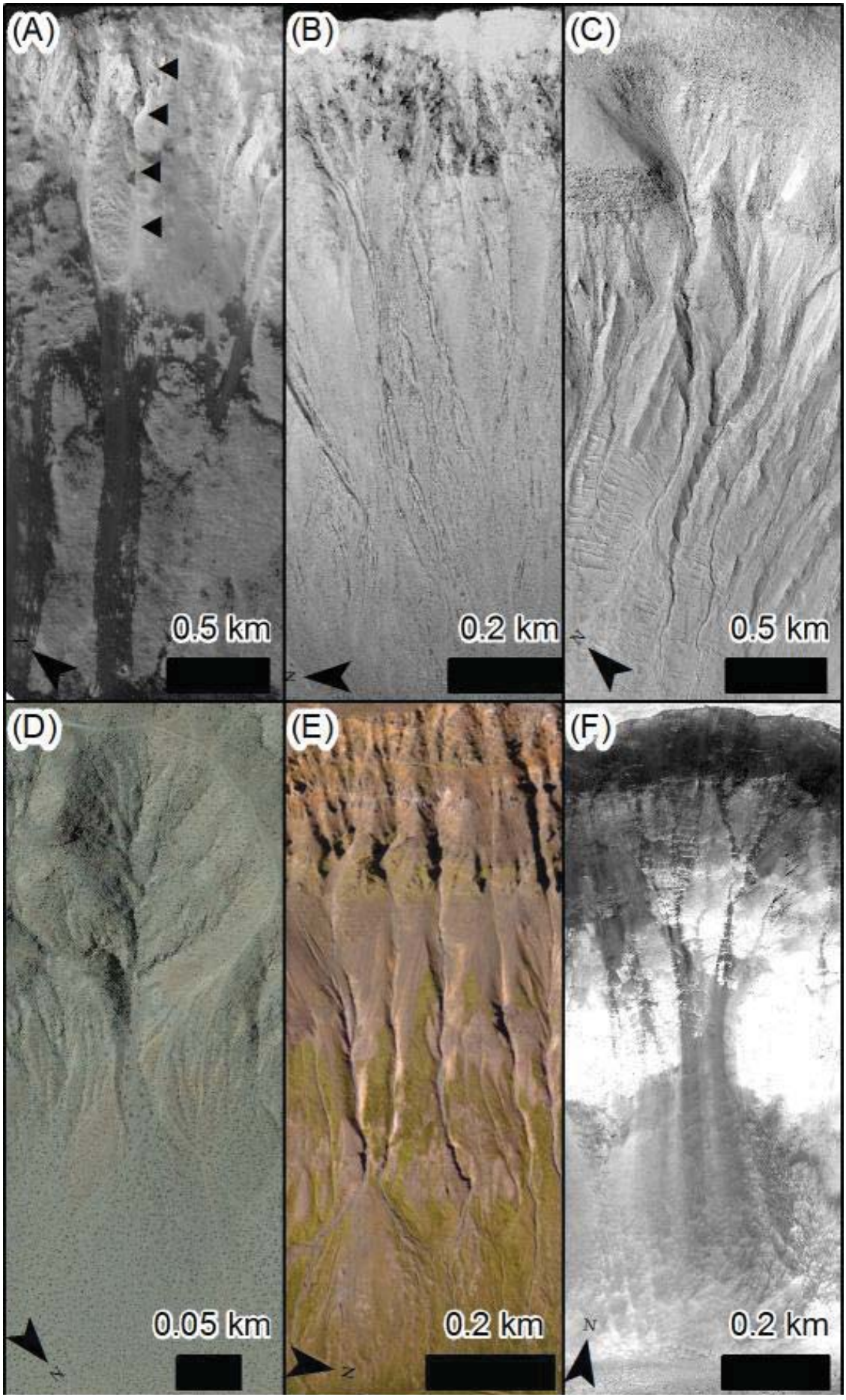

63

Figure 1. Images of gullies on different planets. (A) Gullies on the Moon (arrows indicate the position of the "channel"), LROC image M151169370. Credit: NASA/Goddard Space Flight Center/Arizona State University. (B) Gullies on Mars in an unnamed crater NW of Lyot crater, HiRISE image ESP_027231_2340. Credit: NASA/JPL/University of Arizona. (C) Gullies in Palikir Crater on Mars, HiRISE image PSP_005943_1380. Credit: NASA/JPL/University of Arizona. (D) Ephemeral fluvial gully in Anderson Dry Lake, California on Earth – image from google Earth. (E) Gullies on the eastern flank of Tindastóll Mountain, Iceland, Earth. Aerial image from NERC ARSF. (F) Talus slopes on the south-facing wall of Quebrada Camarones in the Atacama Desert northern Chile. Orthorectified GeoEye image at 0.5 m/pix.

Here we go beyond plan-view comparisons of morphology, such as those illustrated inFig. 1, by examining the three-dimensional properties of terrestrial, lunar and martian gullies. The inspiration for this study came from the delimitation of process-domains from digital elevation models of fluvial catchments on Earth. Montgomery and Foufoula-Georgiou (1993) calculated upslope drainage area and local slope for elevation data-pixels within fluvial catchments and showed that these properties follow a specific pattern in log-log space that depends on which processes were active in the catchment. They included process domains for fluvial and debris flow processes. We have further developed this approach by including other terrain attributes that can discriminate between processes such as cumulative area distribution, area distribution and 25 m downslope index, and by including dry granular flows (rockfalls, ravel and dry mass wasting) as an end-member process. Such hydrological analyses are not typically performed at the scale of the martian gullies (i.e. <5 km) because the data were not historically available. In an earlier study (Conway et al., 2011a) though, we showed that a qualitative comparison of slope-area and cumulative area distribution plots

could discriminate between terrains dominated by debris flow, rockfall and fluvial processes on Earth at this scale. In the current study, we find that differences are also apparent in area distribution, and 25m downslope index plots, as illustrated in Fig. 2. We extend our previous work by analyzing additional sites, including the Moon, and, more importantly, by performing a statistical analysis of the data.

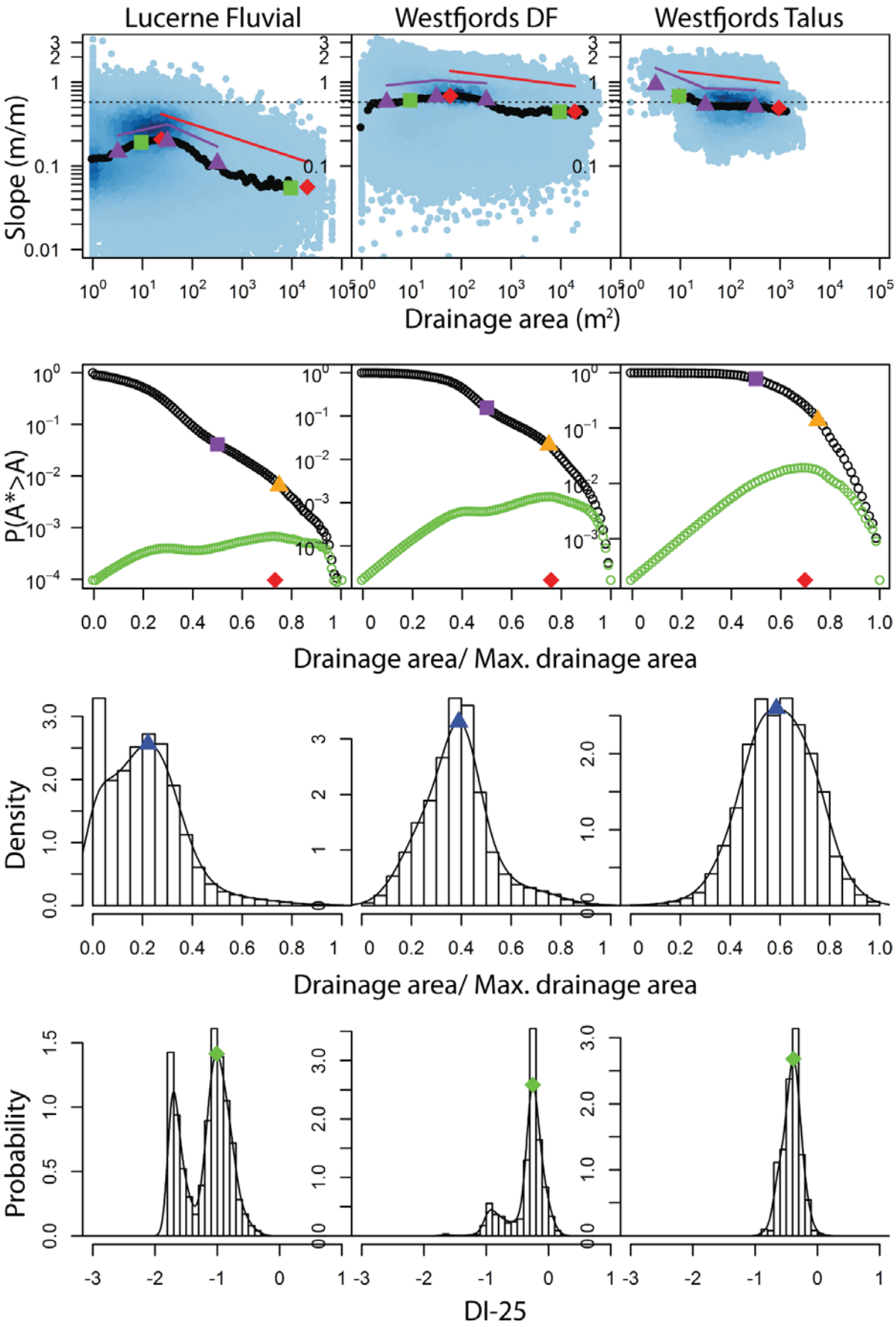
Lucerne Fluvial
Westfjords DF
Westfjords Talus
Slope (m/m)
Drainage area (m²)
P(A*>A)
Drainage area/ Max. drainage area
Density
Drainage area/ Max. drainage area
Probability
DI-25

95

Figure 2. Example terrain analysis plots for sites classed as fluvial, debris flow (DF) and talus on Earth from study sites in Lucerne Valley California and the Westfjords in Iceland (see Supplementary Text and Table S2 for further details). to the first row are slope-area plots, to the second cumulative area distribution plots, the third area distribution plots and the fourth 25 m downslope index plots. The darker shades of the underlying points in the slope-area plots indicates a greater density of points. The dotted line in the slope-area plot is at 30° slope – the approximate minimum dry angle of repose. Some of the parameters listed in Table 1 are marked as follows: (1) in the slope-area plots (top row) the purple triangles are (from left to right): avslp_1_10, avslp_10_100 and avslp_100_1000; the green squares are: left, slp10 and right, slp10_4; the red diamonds are mxslp and mxslpA, located at the maxima, and mxfacslp located at the furthest right; the red line represents gradMax_all vertically displaced for clarity, and the purple lines represent (from left to right), grad100_10 and grad100_1000 vertically displaced for clarity. (2) In the cumulative area distribution plots (2nd row from top), the purple square represents CAD50pc, the yellow triangle CAD75pc and the red diamond maxArCAD. The green points represent a rotated cumulative area distribution plot, made in order to calculate maxDCad, maxArCAD and areaUCad. In order to rotate the cumulative area distribution plot as illustrated, we calculated the straight line that connected the first and the last point, and then subtracted the y-value of this line from every point in the plot. (3) In the area distribution plots (3rd row from top) the blue triangle represents mxCadPkh and mxCadPkFac. (4) In the 25m downslope index plots (bottom row) the green diamond represents maxDi25pkH and mxDi25pkFac.

2.0 Development of Parameterization Scheme

2.1 Hydrological analysis

The datasets used are fully described in the Supplementary Text, summarized in Tables S1 and S2. We followed the same approach as Conway et al. (2011a) in generating the terrain attributes necessary for these analyses and a visual summary of these calculations is shown in Figure S3. In brief, we used the multi-direction flow algorithm "dinf" which partitions flow into downslope neighbors in any direction (Tarboton, 1997). From these non-integer flow directions we calculated the (fractional) number of pixels located upstream of any given pixel, from which we calculated the uphill drainage area (Fig. S3D). Local slope (Fig. S3C) was calculated by taking the steepest of the eight triangular facets centered on the target pixel (Tarboton, 1997). The wetness index maps (Fig. S3A) were calculated by taking the natural logarithm of the ratio of drainage area to slope, excluding pixels with zero slope. We also calculated the flow directions and local slopes using the classic "d8" algorithm whereby flow is routed directly to a single downslope pixel, in one of the eight cardinal directions (O'Callaghan and Mark, 1984). From the d8 flow directions we calculated the distance downflow it is necessary to travel to achieve a given value of descent – the downslope index (Hjerdt et al., 2004) (Fig. S3F). If the value of descent is fixed at or near the DEM resolution, then the downslope index simply represents the steepest downstream slope. Conversely, if values are chosen which are of the same vertical scale as the feature being studied (~500 m for gullies), then within-feature detail is lost. We chose value of descent of 25 m, as a balance between these two end-members. These manipulations were performed using the freely available software packages TauDEM tools (Tarboton, 1997; Tesfa et al., 2011) and WhiteboxGAT (Lindsay, 2005).

2.2 Generating hydrological plots and parameters

The slope-area and cumulative area distribution plots were created following the method of Conway et al. (2011a). Briefly, the slope-area comprises the local slope and drainage area for every pixel plotted in log-log space, and these data are put into 0.05 wide log-drainage-area bins and for each bin the slope is averaged. Bins with less than 100 points are excluded to avoid bias of the mean by outlying datapoints, an approach employed commonly in other studies (e.g., Grieve et al., 2016). For the cumulative area distribution, the same bins are used, but the cumulative frequency for each bin is calculated. The non-cumulative area distribution plot is simply the histogram of the values of the logarithm of the drainage areas normalized by the maximum drainage area. The bin-width is 0.05. The curve is the kernel density estimation of the same distribution with a bandwidth of 0.05. The 25m downslope index plot is similarly the histogram of the logarithm of the 25m downslope index values with a 0.1 bin-width and the line is the corresponding kernel density with a bandwidth of 0.075.

For the area distribution and 25m downslope index plots the number of peaks was calculated by counting the number of maximum inflections on the curve. The area under the tallest peak was calculated by integrating the curve between the minima on either side of the peak.

2.3 Statistical analysis of terrain attributes

In order to analyze a given hillslope, we outlined the feature of interest from the upper watershed boundary to the toe of the deposit-fan or lobes with the aid of hillshaded relief and wetness index maps. All the pixels from the slope, drainage area, and 25m downslope index grids that fell within these polygon outlines were extracted in order to create the slope-area, cumulative area distribution, area distribution and 25m downslope index plots. Instead of

subjectively comparing these plots (as in Conway et al., 2011a), we parameterized the slope-area, cumulative area distribution, area distribution and 25m downslope index plots, to allow quantitative comparison. From visual inspection of the slope-area, cumulative area distribution, area distribution and 25m downslope index plots of our terrestrial sites, and which are dominated by different processes, we noticed that they had qualitatively different shapes and trends, as illustrated by typical "process type" examples in Fig. 2. This was an observation we made in Conway et al. (2011a) and has already been discussed in detail in previous publications for the slope-area and cumulative area distribution plots (e.g., Brardinoni and Hassan, 2006; Lague and Davy, 2003; McNamara et al., 2006; Montgomery and Foufoula-Georgiou, 1993; Perera and Willgoose, 1998). For example, Lague and Davy (2003) noted that a shallower slope at <1 km^2 drainage area in the slope-area plot indicated debris flow dominance in the system and McNamara et al. (2006) noted that concavity in the cumulative area distribution plots indicates a transition from diffusive hillslopes to channel incision.

We therefore extracted 28 parameters that we observed to vary with process from inspection of the plots from our terrestrial sites, informed by trends noted in the literature. Some of these parameters are highlighted in Fig. 2. These include the slope of the trend in the slope-area plot, the concavity of the cumulative area distribution plot, the skewness of the area distribution and the number of peaks in the 25m downslope index plot; the full list of parameters is given in Table 1. Not all these parameters have a clearly describable physical meaning, they were chosen only because they appeared to discriminate between process.

Using these 28 parameters, we performed canonical discriminant analysis (McLachlan, 2004), a statistical technique which produces a linear combination of the parameters which best separate pre-defined groups. This analysis allows assessment of

whether certain groups are separable, and identification of those parameters which are more important in separating the groups.

We analyzed the topography of 104 sites (in 26 locations): 13 on the Moon, and 55 on Earth, including 15 slopes presently dominated by fluvial processes, 27 by debris flow and 13 by dry processes, including rockfall, grainflow and ravel. Unfortunately, data of sufficient resolution are not available to perform this kind of analysis for the proposed gully-like features on Vesta (Scully et al., 2015). On Mars, we obtained data from 33 slopes with gullies, and three without (in 'Zumba' Crater). We examined martian gully sites from a wide spread of latitude (53°N to 68°S) and longitude (0-360°E) to sample a diverse group of gullies. We did not include martian "gullies" formed in sand dunes slipfaces (e.g., Diniega et al., 2013; Mangold et al., 2003; Pasquon et al., 2016; Reiss and Jaumann, 2003). For data-sources, resolutions and locations see Fig. S2, Tables S1-S2 and the Supplementary Text.

203 **Table 1.** Summary of parameters extracted from the hydrological plots.[a]

Parameter abbreviation	Plot derived from	Description	Symbol on Fig. 2	Standardized canonical coefficients					Mean value per group			
				A1	A2	A3	B1	B2	fl	df	rf	mn
mxslp	S-A	the maximum value of slope along the moving average line	red diamond	-1.11	-1.68	-2.54	0.99	2.79	0.452	0.882	0.916	0.891
mxslpA	S-A	the drainage area at which mxslp occurs	red diamond	-0.43	-0.17	-0.35	0.31	0.32	15.954	11.392	6502.426	7.499
slp10	S-A	the value of the moving average line at a drainage area of 10 m^2, if there are fewer than 100 datapoints in this bin is expaned to $10^1 \pm 10^{0.2}$	green square	-0.19	1.47	1.19	-0.39	-1.88	0.407	0.772	0.635	0.823
slp10_4	S-A	the value of the moving average line at a drainage area of 10^4 m^2, if there are fewer than 100 datapoints in this bin is expaned to $10^4 \pm 10^{0.2}$	green square	-0.24	-0.07	0.87	0.49	-0.65	0.196	0.453	0.480	0.510
avslp_1_10	S-A	The mean value of the slope in the range 1 to 10 m^2	purple triangle	0.42	0.88	2.02	-0.19	-2.09	0.378	0.753	0.625	0.794
avslp_10_100	S-A	The mean value of the slope in the range 10 to 100 m^2	purple triangle	0.67	1.52	2.02	-0.76	-2.38	0.395	0.681	0.626	0.702
avslp_100_1000	S-A	The mean value of the slope in the range 100 to 1000 m^2	purple triangle	0.68	-1.29	-1.89	-0.31	2.42	0.286	0.559	0.545	0.641
mxfacslp	S-A	The mean value of the slope in the range spanning the maximum drainge area recorded (maxFac) and maxFac - 10^1	red diamond	0.44	1.45	-1.38	-1.67	0.21	0.158	0.419	0.493	0.431
grad100_10	S-A	The slope of the line connecting avslp_1_10 with avslp_10_100	purple line	0.52	-1.48	-0.86	0.30	1.83	-0.030	0.023	-0.173	0.058
grad100_1000	S-A	The slope of the line connecting avslp_10_100 with avslp_100_1000	purple line	0.36	-1.12	-1.16	0.06	1.61	0.157	0.085	0.041	0.036
gradMax_10_4	S-A	The slope of the line connecting mxslp with slp10_4	not marked	0.09	0.51	-0.62	-0.57	0.16	-0.140	-0.087	-0.062	-0.077
gradMax_all	S-A	The slope of the line connecting mxslp with mxfacslp	red line	0.43	-0.46	0.58	0.17	-0.09	-0.144	-0.090	-0.089	-0.084
CAD50pc	CAD	The value of the probability at a fractional drainage area of 0.5	purple square	0.25	-0.77	-1.46	-0.18	1.64	-1.202	-0.844	-0.319	-0.247
CAD75pc	CAD	The value of the probability at a fractional drainage area of 0.75	yellow triangle	-1.30	-0.27	0.47	1.23	-0.38	-1.857	-1.737	-1.334	-1.322
cad1000	CAD	The value of the probability at an absolute drainage area of 1000 m^2	not marked	1.37	-0.19	0.61	-0.78	-0.18	-1.510	-1.212	-0.928	-0.372
maxDCad	CAD	The height of the tallest point in the rotated CAD plot	not marked	-0.64	-3.01	-1.56	1.85	3.05	0.955	1.582	2.053	2.444
maxArCAD	CAD	The fractional drainage area at which maxDCad occurs	red diamond	0.06	-0.07	-0.27	-0.08	0.25	0.816	0.725	0.687	0.683
areaUCad	CAD	The area underneath the rotated CAD plot	not marked	0.19	3.13	2.05	-1.39	-3.46	0.293	0.540	0.628	0.674
mxCadPkh	AD	The height of the tallest peak in the AD plot	blue triangle	0.15	0.42	0.27	-0.28	-0.44	2.636	2.696	2.781	2.553
mxCadPkFac	AD	The fractional drainage area at which mxCadPkh occurs	blue triangle	0.44	-0.67	-0.27	0.02	0.74	1.484	2.151	3.209	3.681
nrCadPks	AD	The number of peaks in the AD plot	not marked	0.03	0.49	-0.02	-0.33	-0.29	1.200	1.000	1.118	1.077
cadPkArea	AD	The area underneath the tallest peak in the AD plot	not marked	-0.10	0.25	0.27	0.01	-0.38	0.999	1.001	0.974	1.001
cadSkew	AD	The skew of the AD distribution	not marked	-0.62	-1.19	-0.40	1.13	1.03	1.279	0.597	0.073	-0.366
maxDi25pkH	DI25	The height of the tallest peak in the DI25 plot	green diamond	-0.05	-0.48	0.19	0.49	0.18	1.508	2.000	2.457	3.345
mxDi25pkFac	DI25	The fractional drainage area at which mxDi25pkH occurs	green diamond	0.00	-0.37	0.41	0.36	-0.08	0.419	0.646	0.588	0.657
maxDi25pkA	DI25	The area underneath the tallest peak in the DI25 plot	not marked	0.21	0.01	0.29	-0.06	-0.20	0.644	0.861	0.910	0.993
di25Skew	DI25	The skew of the DI25 distribution	not marked	-0.34	-0.33	0.02	0.47	0.14	-0.610	-0.864	-1.028	-1.905
di25bim	DI25	Degree of bimodality of the DI25 distribution	not marked	0.08	-0.44	-0.05	0.20	0.32	0.045	0.011	0.008	0.002

[a]Data from two different canonical discriminant analyses are shown, A1, A2 and A3 are the standardized canonical coefficients from an analysis which best separates terrestrial fluvial, terrestrial debris flow, dry mass wasting on Earth and dry mass wasting from the Moon. Function A1 accounts for 65% of the variation, A2 24% and A3 10%. B1 and B2 are the standardized canonical coefficients from an analysis which best separates terrestrial fluvial, terrestrial debris flow and dry mass wasting (grouping data from the Moon and Earth). Function B1 accounts for 72% of the variation and B2 23%. Absolute values of standardized canonical coefficients greater than one are marked in light grey and those greater than two in dark grey; parameters where any of the standardized canonical coefficients exceed one or two are marked in the same way. For the four columns on the right of the table the values are mean values for each group, where "fl" is terrestrial fluvial, "df" is terrestrial debris flow, "rf" is terrestrial rockfall, and "mn" is lunar.

First, we performed an analysis to best-separate terrestrial fluvial, debris flow, rockfall and lunar slopes (analysis "A"). Second, we grouped rockfall slopes on Earth with lunar slopes and re-performed the analysis (analysis "B"). We choose these specific groupings, because these allowed us to create parameter space plots in which different regions correspond to different gully-forming processes. We performed two analyses because we wanted to confirm whether the inherent differences between the slopes with dry mass wasting on the Earth (which are inevitably influenced by some water) and on the Moon (which are completely dry) affected the process and thus the separation of the groupings. Finally, we added the martian data onto these parameter spaces to see where they plotted. We estimated the range of the adjustment to the martian data needed for reduced gravity conditions. Due to the martian gully processes being unknown at this stage of the analysis, no unequivocal gravity correction could be made, only an estimate of the range of possible

229 corrections (see Section 2.5). The effects of the range of possible corrections are shown as
230 lines extending from the martian gully data points in Fig. 3. We also performed a sensitivity
231 analysis to test the robustness of our analysis, which is illustrated by the ellipses in Fig. 3 and
232 is fully detailed in the Supplementary Text and in Fig. S1.

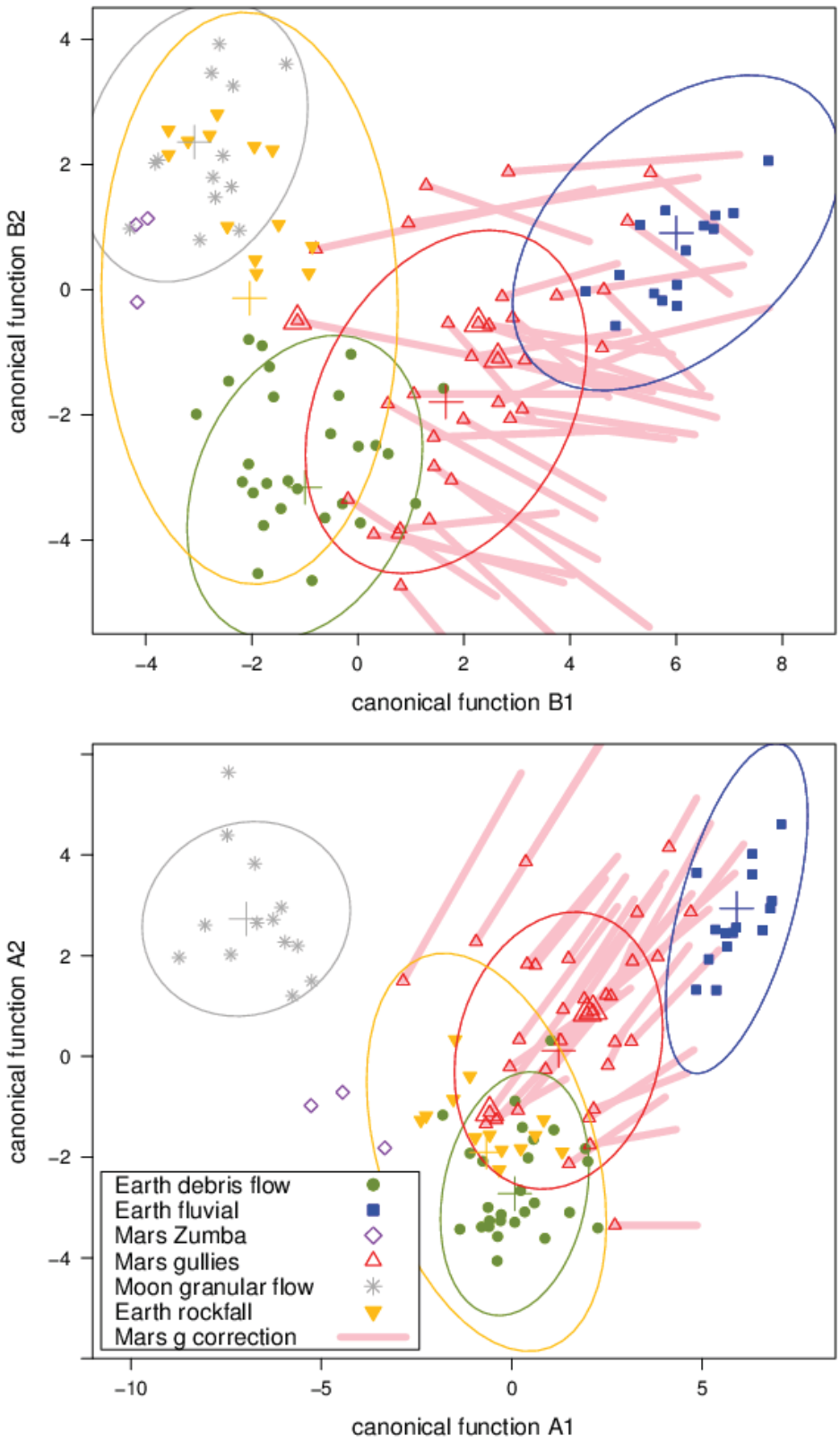

Figure 3. Results of the canonical discriminant analyses. Points labelled as "Zumba Crater" are located on martian slopes without gullies, but with evidence of mass wasting. The ellipses are the 68% confidence interval for the corresponding color group in the legend, with the

cross being the mean value – both take into account the datapoints shown here and also those data from the error analyses detailed in the Supplementary Text and Fig. S1. Top: plot of the first two canonical functions (A1 and A2) which best separate terrestrial fluvial, terrestrial debris flow, lunar slopes and terrestrial rockfall. Bottom: plot of the two canonical functions (B1 and B2) which best separate terrestrial fluvial, terrestrial debris flow and grouped lunar slopes and terrestrial rockfall slopes. The lines extending away from the martian gully datapoints indicate the direction in which the data would shift if the effect of reduced martian gravity is taken into account. However, because of the uncertainty of process in martian gullies we cannot give an exact magnitude for this shift (see Section 2.5). The double-triangles on three of the martian datapoints indicate three catchments in Istok crater where debris flow morphologies have been identified by Johnsson et al. (2014). The canonical coefficients which make up the canonical functions A1, A2, B1 and B2 are given in Table 1.

2.4 Gravity scaling

To account for the difference between terrestrial and martian gravity, a process has to be assigned to a system in order to infer the effect on the landscape. The equations governing that process can then be used to estimate the effect it has on the landscape. Here, we explain our rationale for applying gravity scaling to (i) dry mass wasting, (ii) fluid flows (including fluvial processes, debris flow and fluidized granular flow).

For dry granular flows some authors have found that the dynamic angle of repose is independent of gravity (Atwood-Stone and McEwen, 2013), whereas others have found that it reduces by ~10° (Kleinhans et al., 2011) under martian gravity. We find no significant difference between the slope angle of loose material on the walls of fresh impact craters on the Moon, talus slopes on Mars and talus on Earth, as demonstrated in Fig. 4; hence we assume that any piled loose material should come to rest at the same angle on Mars as on the

Earth. Therefore we make no adjustment to the terrain analysis plots to account for the effect of changing the gravitational acceleration on dry mass wasting processes.

For clear water flows eroding into bedrock (detachment limited), the erosion rate in volume per unit channel area per time is a power law function of the basal shear stress (Snyder et al., 2000; e.g., Whipple and Tucker, 1999), the so-called "stream-power law":

$$E = k_b \tau^a \quad (1)$$

where k_b is a dimensional coefficient dependent on rock resistance, dominant erosion process and sediment load, and a is a positive, process-dependent constant (the reciprocal of the Hack exponent). Previous analyses (Irwin et al., 2005; Som et al., 2009) have revealed that, for the same discharge (which should scale with drainage area) and slope, channels on Mars should be larger than their terrestrial equivalents in order to compensate for the reduced velocity under reduced gravity. If we instead fix the channel dimensions, then channels of the same dimensions will be found on higher slopes on Mars compared to Earth. As fluvial channel initiation can be considered as a result of exceeding a critical velocity, or shear stress (Horton, 1945; Moore et al., 1988) then, on Mars for any given drainage area (discharge), the slope would need to be higher compared to Earth, everything else being equal. This was also suggested by the analysis and data of Lanza et al. (2010). Conway et al. (2011a) find that the appropriate slope-shift for equilibrium bedrock fluvial erosion under steady-state uplift conditions in slope-area plots, for a given drainage area, should be +1/3. However, they did not take into account the potential effects of g on the dimensional constants, which should somewhat counteract this shift. Therefore in our analyses we take the shift of 1/3 as the extreme value.

When the bedload cover of the flow is taken into account (transport limited), there are a number of different formulations of the stream power law; many take a form similar to (Densmore et al., 1998; Lavé and Avouac, 2001):

$$E = K\,(\tau^* - \tau^*_c) \quad (2)$$

where K is an erodibility coefficient, τ^* is given by τ / (ρ_s – ρ) g D_{50} and τ^*_c is a Shield's-Stress-like threshold dimensionless shear stress, where ρ_s is the density of the grains and D_{50} is their modal size. In this case, because τ^* has g in the denominator and in the numerator (from Eq. 1), there is no effect on erosion rate of changing gravity.

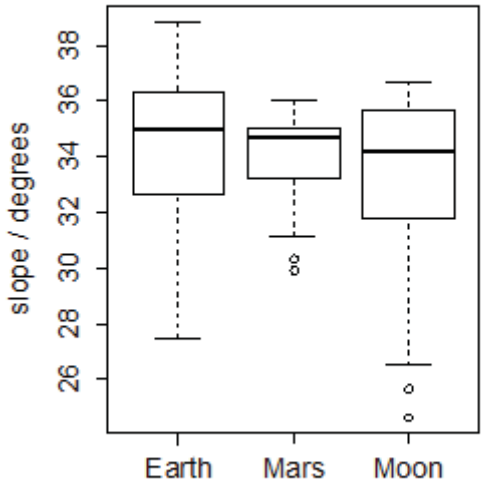

Figure 4. Box plots of measurements of the slope of talus on Earth (35), Mars (30) and the Moon (22). The bar across each box is the median value, the extent of the box delimits the interquartile range, and the whiskers indicate the range, while the points are outliers - values which are further than 1.5 interquartile ranges from the quartiles. Each measurement was taken over a span of ~50 m on part of the hillslope that was smooth or contained loose boulders within the image. On Earth ten measurements were taken in the Westfjords, ten in St. Elias and 15 in Quebrada de Camarones. On Mars, ten measurements were taken in Zumba Crater, ten on the north-facing slope of Istok Crater and ten in Juventae Chasma (DT1EA_003434_1755_003579_1755_U01, credit USGS). On the Moon ten measurements were taken in "Unnamed Fresh Crater West of Isaev Crater", seven in "Unnamed Fresh

303 Crater West of Saenger" and five in Moore F Crater (NAC_DTM_MOOREF1_E370N1850,
304 credit Arizona State University).
305
306 For debris flows, if we assume for simplicity a single fluid rheology, then there are
307 two possible modes. Firstly, the case of an erodible non-cohesive bed, where the erosion rate
308 is determined by the flow's ability to erode grains. This is determined by a critical shear
309 stress:
310 $$\tau_{c} = (\rho_s - \rho)\, g\, D_{50} \cos\theta \quad (3)$$
311 The ratio of the bed shear stress (Eq. 1) to the critical shear stress (Eq. 3) is a constant given
312 by:
313 $$\tau / \tau_c = \rho\ H \tan\theta / [(\rho_s - \rho)\, D_{50}] \quad (4)$$
314 which is not dependent on gravity. Secondly, where the bed is cohesive, the critical shear
315 stress becomes a constant, hence the stress required to erode the bed becomes dependent on
316 gravity, and therefore so does the inclination of the bed.
317 This formulation for debris flows is over-simplistic and more complex schemes have
318 been proposed, such as separating the shear-stresses imposed by the granular component and
319 fluid component of the flow (Iverson et al., 2010). In Iverson's formulation the fluid part is a
320 Bingham fluid with a Coulomb-like failure, and the granular part includes a shear stress term
321 similar to Eq. 1 and also a pore-pressure term. Takahashi (1981, 1978) proposed a model
322 informed by Bagnold's concept of dispersive stress included in a water-saturated inertial
323 grain flow, where again a Coulomb-like failure is included. Even in these more complex
324 cases a decrease in gravitation acceleration acts to decrease basal shear stress and never acts
325 to increase it, despite the exact influence being more complicated to calculate.
326 Under a steady-state, these erosion-rate laws can be converted into a change in local
327 slope. However, in ephemeral systems we have studied on Earth (and almost certainly gullies

on Mars are ephemeral), this assumption cannot be made. The erosion rate for both fluvial and debris flow processes can depend on gravitational acceleration. In all cases, this acts to increase the local slope for a given drainage area (as a proxy for discharge) on Mars compared to Earth, even if an assumption of steady-state cannot be made. Hence we conclude that in all cases the adjustment for gravity shown in Fig. 3 has to be in the direction indicated, and is most likely to be at the lower end of the range indicated by the lengths of the lines.

In summary, for a cohesive bed (e.g., bedrock), cohesion dominates gravity, so gravity scaling is required, but a non-cohesive bed, the shear stress required for erosion depends upon the weight of individual particles, so the effects of gravity cancel out. We have no *a priori* knowledge of whether the martian gully beds are cohesive or not, so exact scaling cannot be applied. Instead, to provide an indication of how gravity scaling affects the data in Fig. 3, we use an estimated maximum value of 1/3. This is likely to be an overly exaggerated maximum, as shown by the slope-area analysis of channel initiation in gullies on Mars by Lanza et al. (2010), who find differences in material properties and environmental factors are likely to be more influential on the slope-area data than gravity scaling.

3.0 Interpretations and Discussion

Our earlier study (Conway et al., 2011a) showed that some martian gullies qualitatively resembled terrestrial debris flows in terrain analysis data, and that this was not due to crater-wall topography producing spurious debris-flow like results. For the first time, our new analysis demonstrates quantitatively that, when using terrain parameters that best separate granular flow landforms from fluvial or debris flow landforms, martian gullies overlap the parameter space for both debris flow and fluvial gullies on Earth (Fig. 3). The majority of the martian gully data cluster between the fluvial and debris flow domains, suggesting a blend of processes. Importantly though, our analysis shows that martian gullies have very different

353 topographic properties from slopes with gully-like features on the Moon – a “dry granular
354 flow” analog.

355 Any adjustment to account for the effect of reduced martian gravity, shifts the data
356 further from the lunar slopes and further into the terrestrial fluvial domain, particularly for
357 canonical function A1, with which the martian gullies completely overlap the fluvial domain.
358 However, this transformation shifts martian gullies with identifiable debris flow
359 morphologies (Johnsson et al., 2014) away from the terrestrial debris flow data in Fig. 3. This
360 perhaps suggests that the necessary adjustment for gravity may only be small for debris flow
361 processes, which are one of the best-articulated mechanisms for gullies on Mars (e.g.,
362 Costard et al., 2002; de Haas et al., 2015b).

363 To check the method, we also examined martian slopes without gullies, to confirm
364 that these fall within the domain of dry processes. We found that non-gullied terrain within
365 craters on Mars does not produce signals resembling those of fluvial or debris flows on Earth:
366 the walls of the fresh impact crater Zumba plot between the lunar data and Earth rockfall data
367 on Fig. 3 – in agreement with earlier studies (Conway et al., 2011a). This contrasts to the
368 results of Hobbs et al. (2014), who found that pre-existing topography has a detectable
369 influence on the two-dimensional long profiles of martian gullies. Our analysis shows that,
370 when considered in three dimensions, the shape is dominated by the active process.

371 The spread of the terrestrial data in Fig. 3 reflects not only the inevitable mixing of
372 different process signals, but also the effects of different substrates, including differing
373 amounts and types of bedrock outcrop, soil types and thickness, and vegetation types and
374 cover (see Supplementary Material for full description of the terrestrial sites). The lunar data
375 have a similar scatter, which also probably reflects the geological diversity of the different
376 sample sites, including different geological units, amount of bedrock outcrop, regolith
377 thickness and maturity, presence and amount of impact melt, and amount of ejecta cover.

Similar factors are also likely to be influencing the martian data. Similarly to Earth, many gully alcoves incise into the competent bedrock of their host crater wall (Aston et al., 2011; de Haas et al., 2015a, 2015c; Okubo et al., 2011),, which can have a range of ages, type, weathering state and structure. On Mars, gullies are often incised into a surface-draping unit, called the latitude dependent mantle (LDM; Christensen, 2003; Conway and Balme, 2014; Dickson et al., 2015; Head et al., 2008; Levy et al., 2011), which previous work has interpreted to comprise either massive ice, or ice-rich sediment. None of our terrestrial sites are located on massive ice, but many of them have discontinuous mountain permafrost (Adventdalen, Svalbard; St. Elias, Alaska; Front Range, Colorado; Tindastóll, Iceland), which has similar mechanical behavior to erosion. Although the substrates in the three sites are not strictly analogous, we feel that by choosing a wide variety of sites we have captured enough of the variability of the substrate (i.e., a wide range of cohesion and erodibility) in order to consider substrate as a secondary factor compared to the more dominant effect of process.

The even larger spread of the martian gully data in Fig. 3 compared to the terrestrial and lunar sites reflects a) their variability of form and setting, and b) either catchments with mixed processes, or long periods of quiescence allowing dry processes to gradually overprint other processes. We have included gullies that deeply incise the ice-dust mantle (Conway and Balme, 2014), those in polar pits, isolated gullies, grouped gullies, gullies that form dense coalescing networks, and those that possess thin channels. The systems we have selected on Earth (with the exception of the sites in the Atacama) are almost constantly transforming under the influence of water-driven processes, yet maintain the process signal. On Mars, dry mass-wasting (CO_2-driven, or not), aeolian processes (and perhaps long-term creep) might be expected to modify the topography post-emplacement (de Haas et al., 2015d) and thus

contribute to scatter in the data, yet this has not occurred sufficiently to overprint the process signal.

Another possible cause of the scatter of the data is the potential for metastable water on Mars (Hecht, 2002). On Earth, water is the central component of both fluvial and debris flow processes, but on Mars water can be metastable (Hecht, 2002), being subject to both freezing and boiling, which can change its behavior with respect to stable water (Conway et al., 2011b; Jouannic et al., 2015; Massé et al., 2016). As previous laboratory work has shown, the principle effect of boiling and freezing is to change the infiltration rate – an effect that can be mimicked by changing the properties of the substrate. Therefore we expect that the potential effect of metastability on water on Mars would introduce a variability of the same or lesser magnitude than that of substrate type, which is discussed above.

We discussed briefly in the introduction the possibility that gullies on Mars can be modified, or even formed by CO_2 sublimation driven processes. We consider that dry granular flow is the most analogous of our sampled processes to a putative CO_2 sublimation driven process, because without special circumstances (a confining lid, or inclusion of a large portion of mobile solid CO_2 within the flow) flow triggered by CO_2 sublimation would rapidly loose its pore pressure through gas escape and therefore convert into a non-fluidized dry granular flow. Pyroclastic flows on Earth have been cited to be possible analogues for CO_2 sublimation driven flows (Pilorget and Forget, 2016), yet the energy involved in such flows can be in excess of 10^8 Wm^{-2} (Smil, 2008), tiny in comparison to insolation on Mars (the driver of CO_2 sublimation) which can usually generate < 700 Wm^{-2} even with the most optimal combination of slope, orientation and orbital parameters (Lewis et al., 1999). Cedillo-Flores et al. (2011) estimated that CO_2 sublimation would be sufficient to mobilize sand grains, whose mass is significantly below that of the boulder-grade material often found in gully-deposits on Mars, both old (de Haas et al., 2015d) and new (Dundas et al., 2015).

Pilorget and Forget (2016)'s model, which requires a confining lid of CO_2 slab ice, was optimized for gullies found on sand dunes, but they inferred using analogy to pyroclastic density currents that larger material could be mobilized. Without further modelling, or experimental work to clarify the exact physical transport mechanism involved in CO_2 sublimation driven flows, a detailed discussion would remain highly speculative. However, given the current state of knowledge, we feel that taking dry granular flows as an analogy to putative Mars CO_2-driven flows is reasonable. Using this analogy, our work therefore implies that CO_2 sublimation driven flows are a secondary process influencing the morphology of the non-sand dune martian gullies studied here, and could be a factor in introducing scatter into the data in Fig. 3. For gullies in poorly consolidated sand dune slip faces this process might be dominant, as suggested by recent observations (e.g., Diniega et al., 2013), but this type of gully was not included in this study.

4.0 Conclusions

Our results support the interpretation that liquid water was inherent to the process that formed martian gullies. This conclusion is based upon a new method, yet is in agreement with many other studies that examine the topographic profiles (Conway et al., 2014), morphology (Gallagher et al., 2011; e.g., Johnsson et al., 2014; Levy et al., 2010), and geological and physiographic settings (e.g., Costard et al., 2002; Dickson et al., 2015; Head et al., 2008) of martian gullies. Liquid water must have been available in sufficient quantities to produce this scale of landform, as we argue below.

In terms of the volume of water required, debris flows on Earth are generated by the development of excess pore pressure inside a body of sediment; either produced by over-saturation of the ground by rainfall or snowmelt, or by overland water-flow inside a constraining environment which then infiltrates the sediments - the so-called 'fire-hose'

effect (Johnson and Rodine, 1984). Debris flow initiation is aided by the presence of clay-sized material, which helps to augment pore pressures (Iverson, 1997). Loose surface sediments and fine-fractions are both present on Mars (Cabrol et al., 2014), meaning that debris flow is certainly a plausible process. However, low-volume water flows on Earth cannot produce substantial debris flow, as they are unable to entrain larger particles (de Haas et al., 2014), despite the flows themselves containing more water per unit volume. Substantial boulder-grade materials are often seen within martian gullies (de Haas et al., 2015d). This means that, whether generated by fluvial or debris flow processes, the formation of martian gullies must have involved substantial quantities of water, i.e. centimeters of melt production over the alcove-zone, as calculated in (de Haas et al., 2015c).

Gullies are known to be geologically recent features (Reiss et al., 2004; Schon et al., 2009), so future research should focus on elucidating the timing of gully-forming events with respect to changes in Mars' orbital parameters (and hence possibly climate change; Head et al., 2003), the amounts of water involved, and the mechanism of water-release. Global Climate Models of Mars have so far failed to predict sufficient melting from precipitation to produce gullies under recent (last ~10Ma) climate conditions, hence these results show that we need to revisit our understanding of the recent martian climate. Our work also maintains the designation of gullies as "special regions"(Kminek et al., 2010) under planetary protection rules, whereby the risk of contamination by terrestrial biota is considered too high to be able to send space missions to these regions. It is important not to contaminate these regions, as stratigraphic observations point to intermittent, yet repeated, episodes of activity in gullies (Dickson et al., 2015; Schon and Head, 2011), meaning that they represent intermittently habitable environments and a possible niche for the survival of life on Mars.

Finally, this work reveals that quantifying the 3D shape of landforms opens-up a new avenue for remotely differentiating between dominant processes acting on planetary surfaces.

Although presently such analyses are not widely used, future developments in computational techniques and data processing (e.g., Grieve et al., 2016) promise to make such techniques more widely accessible and usable.

5.0 Acknowledgments

We thank Jay Dickson and one anonymous reviewer for their helpful comments, which greatly improved the manuscript. We acknowledge funding from the Leverhulme Trust in support of this work (grant number RPG-397). This study would not have been possible without data from the UK's Natural Environment Research Council (NERC) Geophysical Equipment Facility loan numbers 977 and 1006, NERC Airborne Research and Survey Facility surveys IPY07-04, EUFAR12-02, European Facility for Airborne Research project "ICELAND_DEBRISFLOWS". We are grateful to the National Science Foundation's National Centre for Airborne Laser Mapping (NSF NCALM) for making available their data through the OpenTopography portal. We acknowledge the freely available tools Taudem (David Tarboton) and WhiteboxGAT (John Lindsay). Valuable feedback was received from Nicolas Warner, David Rothery, Peter Fawdon and John Murray.

6.0 References

Aston, A.H., Conway, S.J., Balme, M.R., 2011. Identifying Martian gully evolution, in: Balme, M., Bargery, A.S., Gallagher, C., Gupta, S. (Eds.), Martian Geomorphology. The Geological Society of London, pp. 151–169.

Atwood-Stone, C., McEwen, A.S., 2013. Avalanche slope angles in low-gravity environments from active Martian sand dunes. Geophys. Res. Lett. 40, 2929–2934. doi:10.1002/grl.50586

501 Balme, M., Mangold, N., Baratoux, D., Costard, F., Gosselin, M., Masson, P., Pinet, P.,
502 Neukum, G., 2006. Orientation and distribution of recent gullies in the southern
503 hemisphere of Mars: Observations from High Resolution Stereo Camera/Mars
504 Express (HRSC/MEX) and Mars Orbiter Camera/Mars Global Surveyor (MOC/MGS)
505 data. J. Geophys. Res. Planets 111, doi:10.1029/2005JE002607.
506 Bart, G.D., 2007. Comparison of small lunar landslides and martian gullies. Icarus 187, 417–
507 421.
508 Brardinoni, F., Hassan, M.A., 2006. Glacial erosion, evolution of river long profiles, and the
509 organization of process domains in mountain drainage basins of coastal British
510 Columbia. J. Geophys. Res. F Earth Surf. 111, doi:10.1029/2005JF000358.
511 Bridges, N.T., Lackner, C.N., 2006. Northern hemisphere Martian gullies and mantled
512 terrain: Implications for near-surface water migration in Mars' recent past. J.
513 Geophys. Res. Planets 111, 9014. doi:10.1029/2006JE002702
514 Cabrol, N.A., Herkenhoff, K., Knoll, A.H., Farmer, J., Arvidson, R., Grin, E., Li, R., Fenton,
515 L., Cohen, B., Bell, J.F., Aileen Yingst, R., 2014. Sands at Gusev Crater, Mars. J.
516 Geophys. Res. Planets doi:10.1002/2013JE004535. doi:10.1002/2013JE004535
517 Cedillo-Flores, Y., Treiman, A.H., Lasue, J., Clifford, S.M., 2011. CO2 gas fluidization in the
518 initiation and formation of Martian polar gullies. Geophys. Res. Lett. 38,
519 doi:10.1029/2011GL049403. doi:10.1029/2011GL049403
520 Christensen, P.R., 2003. Formation of recent martian gullies through melting of extensive
521 water-rich snow deposits. Nature 422, 45–48.
522 Conway, S.J., Balme, M., Murray, J.B., Towner, M.C., Okubo, C., Grindrod, P.M., 2011a.
523 The determination of martian gully formation processes by slope-area analysis., in:
524 Balme, M., Bargery, A.S., Gallagher, C., Gupta, S. (Eds.), Martian Geomorphology.
525 The Geological Society of London, pp. 171–201.

526 Conway, S.J., Balme, M.R., 2014. Decametre-thick remnant glacial ice deposits on Mars.
527 Geophys. Res. Lett. 41, 5402–5409. doi:10.1002/2014GL060314
528 Conway, S.J., Balme, M.R., Lamb, M.P., Towner, M.C., Murray, J.B., 2011b. Enhanced
529 runout and erosion by overland flow under subfreezing and low pressure conditions:
530 experiments and application to Mars. Icarus 211, 443–457.
531 doi:10.1016/j.icarus.2010.08.026
532 Conway, S.J., Balme, M.R., Murray, J.B., Towner, M.C., 2014. A Signal for Water on Mars:
533 The Comparison of Topographic Long Profiles of Gullies on Earth to Gullies on
534 Mars. Lunar Planet. Sci. Conf. 45, # 2438.
535 Costard, F., Forget, F., Mangold, N., Peulvast, J.P., 2002. Formation of recent Martian debris
536 flows by melting of near-surface ground ice at high obliquity. Science 295, 110–113.
537 doi:10.1126/science.1066698
538 de Haas, T., Conway, S.J., Krautblatter, M., 2015a. Recent (Late Amazonian) enhanced
539 backweathering rates on Mars: paracratering evidence from gully-alcoves? J.
540 Geophys. Res. Planets 120, 2169–2189. doi:10.1002/2015JE004915
541 de Haas, T., Hauber, E., Conway, S.J., Van Steijn, H., Johnsson, A., Kleinhans, M.G., 2015b.
542 Earth-like aqueous debris-flow activity on Mars at high orbital obliquity in the last
543 million years. Nat. Commun. in press. doi:10.1038/ncomms8543
544 de Haas, T., Hauber, E., Conway, S.J., van Steijn, H., Johnsson, A., Kleinhans, M.G., 2015c.
545 Earth-like aqueous debris-flow activity on Mars at high orbital obliquity in the last
546 million years. Nat. Commun. 6.
547 de Haas, T., Ventra, D., Carbonneau, P., Kleinhans, M.G., 2014. Debris-flow dominance of
548 alluvial fans masked by runoff reworking and weathering. Geomorphology 217, 165–
549 181. doi:10.1016/j.geomorph.2014.04.028

de Haas, T., Ventra, D., Hauber, E., Conway, S.J., Kleinhans, M.G., 2015d. Sedimentological analyses of martian gullies: The subsurface as the key to the surface. Icarus 258, 92–108. doi:10.1016/j.icarus.2015.06.017

Densmore, A.L., Ellis, M.A., Anderson, R.S., 1998. Landsliding and the evolution of normal-fault-bounded mountains. J. Geophys. Res. Solid Earth 103, 15203–15219. doi:10.1029/98JB00510

Dickson, J.L., Head, J.W., Goudge, T.A., Barbieri, L., 2015. Recent climate cycles on Mars: Stratigraphic relationships between multiple generations of gullies and the latitude dependent mantle. Icarus 252, 83–94. doi:10.1016/j.icarus.2014.12.035

Dickson, J.L., Head, J.W., Kreslavsky, M., 2007. Martian gullies in the southern mid-latitudes of Mars: Evidence for climate-controlled formation of young fluvial features based upon local and global topography. Icarus 188, 315–323.

Diniega, S., Hansen, C.J., McElwaine, J.N., Hugenholtz, C.H., Dundas, C.M., McEwen, A.S., Bourke, M.C., 2013. A new dry hypothesis for the formation of martian linear gullies. Icarus 225, 526–537. doi:10.1016/j.icarus.2013.04.006

Dundas, C.M., Diniega, S., Hansen, C.J., Byrne, S., McEwen, A.S., 2012. Seasonal activity and morphological changes in martian gullies. Icarus 220, 124–143. doi:10.1016/j.icarus.2012.04.005

Dundas, C.M., Diniega, S., McEwen, A.S., 2015. Long-Term Monitoring of Martian Gully Formation and Evolution with MRO/HiRISE. Icarus 251, 244–263. doi:10.1016/j.icarus.2014.05.013

Dundas, C.M., McEwen, A.S., Diniega, S., Byrne, S., Martinez-Alonso, S., 2010. New and recent gully activity on Mars as seen by HiRISE. Geophys. Res. Lett. 37, doi:10.1029/2009gl041351. doi:10.1029/2009gl041351

Gallagher, C., Balme, M.R., Conway, S.J., Grindrod, P.M., 2011. Sorted clastic stripes, lobes and associated gullies in high-latitude craters on Mars: Landforms indicative of very recent, polycyclic ground-ice thaw and liquid flows. Icarus 211, 458–471. doi:10.1016/j.icarus.2010.09.010

Grieve, S.W.D., Mudd, S.M., Hurst, M.D., Milodowski, D.T., 2016. A nondimensional framework for exploring the relief structure of landscapes. Earth Surf Dynam 4, 309–325. doi:10.5194/esurf-4-309-2016

Harrison, T.N., Osinski, G.R., Tornabene, L.L., Jones, E., 2015. Global Documentation of Gullies with the Mars Reconnaissance Orbiter Context Camera and Implications for Their Formation. Icarus 252, 236–254. doi:10.1016/j.icarus.2015.01.022

Head, J.W., Marchant, D.R., Kreslavsky, M.A., 2008. Formation of gullies on Mars: Link to recent climate history and insolation microenvironments implicate surface water flow origin. Proc. Natl. Acad. Sci. U. S. A. 105, 13258–13263.

Head, J.W., Mustard, J.F., Kreslavsky, M.A., Milliken, R.E., Marchant, D.R., 2003. Recent ice ages on Mars. Nature 426, 797–802. doi:10.1038/nature02114

Hecht, M.H., 2002. Metastability of liquid water on Mars. Icarus 156, 373–386.

Heldmann, J.L., Carlsson, E., Johansson, H., Mellon, M.T., Toon, O.B., 2007. Observations of martian gullies and constraints on potential formation mechanisms II. The northern hemisphere. Icarus 188, 324–344.

Heldmann, J.L., Mellon, M.T., 2004. Observations of martian gullies and constraints on potential formation mechanisms. Icarus 168, 285–304.

Hjerdt, K.N., McDonnell, J.J., Seibert, J., Rodhe, A., 2004. A new topographic index to quantify downslope controls on local drainage. Water Resour. Res. 40, doi:10.1029/2004WR003130.

598 Hobbs, S.W., Paull, D.J., Clark, J.D.A., 2014. A comparison of semiarid and subhumid
599 terrestrial gullies with gullies on Mars: Implications for Martian gully erosion.
600 Geomorphology 204, 344–365. doi:10.1016/j.geomorph.2013.08.018
601 Horton, R.E., 1945. Erosional development of streams and their drainage basins;
602 hydrophysical approach to quantitative morphology. Geol. Soc. Am. Bull. 56, 275–
603 370. doi:10.1130/0016-7606(1945)56[275:edosat]2.0.co;2
604 Irwin, R.P., Craddock, R.A., Howard, A.D., 2005. Interior channels in Martian valley
605 networks: Discharge and runoff production. Geology 33, 489–492.
606 doi:10.1130/G21333.1
607 Iverson, R.M., 1997. The physics of debris flows. Rev Geophys 35, 245–296.
608 Iverson, R.M., Logan, M., LaHusen, R.G., Berti, M., 2010. The perfect debris flow?
609 Aggregated results from 28 large-scale experiments. J. Geophys. Res. - Earth Surf. J.
610 Geophys. Res. F Earth Surf. 115, doi:10.1029/2009JF001514.
611 Johnson, A.M., Rodine, J.R., 1984. Debris flow., in: Brunsden, D., Prior, D.B. (Eds.), Slope
612 Instability. Wiley, Chichester, pp. 257–357.
613 Johnsson, A., Reiss, D., Hauber, E., Hiesinger, H., Zanetti, M., 2014. Evidence for very
614 recent melt-water and debris flow activity in gullies in a young mid-latitude crater on
615 Mars. Icarus 235, 37–54. doi:10.1016/j.icarus.2014.03.005
616 Jouannic, G., Gargani, J., Conway, S.J., Costard, F., Balme, M.R., Patel, M.R., Massé, M.,
617 Marmo, C., Jomelli, V., Ori, G.G., 2015. Laboratory simulation of debris flows over
618 sand dunes: Insights into gully-formation (Mars). Geomorphology 231, 101–115.
619 doi:10.1016/j.geomorph.2014.12.007
620 Kleinhans, M.G., Markies, H., de Vet, S.J., in ’t Veld, A.C., Postema, F.N., 2011. Static and
621 dynamic angles of repose in loose granular materials under reduced gravity. J.
622 Geophys. Res. Planets 116, doi:10.1029/2011JE003865. doi:10.1029/2011JE003865

623 Kminek, G., Rummel, J.D., Cockell, C.S., Atlas, R., Barlow, N., Beaty, D., Boynton, W.,
624 Carr, M., Clifford, S., Conley, C.A., Davila, A.F., Debus, A., Doran, P., Hecht, M.,
625 Heldmann, J., Helbert, J., Hipkin, V., Horneck, G., Kieft, T.L., Klingelhoefer, G.,
626 Meyer, M., Newsom, H., Ori, G.G., Parnell, J., Prieur, D., Raulin, F., Schulze-
627 Makuch, D., Spry, J.A., Stabekis, P.E., Stackebrandt, E., Vago, J., Viso, M., Voytek,
628 M., Wells, L., Westall, F., 2010. Report of the COSPAR mars special regions
629 colloquium. Life Sci. Space 46, 811–829. doi:10.1016/j.asr.2010.04.039
630 Kneissl, T., Reiss, D., van Gasselt, S., Neukum, G., 2010. Distribution and orientation of
631 northern-hemisphere gullies on Mars from the evaluation of HRSC and MOC-NA
632 data. Earth Planet. Sci. Lett. 294, 357–367. doi:j.epsl.2009.05.018
633 Krohn, K., Jaumann, R., Otto, K., Hoogenboom, T., Wagner, R., Buczkowski, D.L., Garry,
634 B., Williams, D.A., Yingst, R.A., Scully, J., De Sanctis, M.C., Kneissl, T.,
635 Schmedemann, N., Kersten, E., Stephan, K., Matz, K.-D., Pieters, C.M., Preusker, F.,
636 Roatsch, T., Schenk, P., Russell, C.T., Raymond, C.A., 2014. Mass movement on
637 Vesta at steep scarps and crater rims. Icarus 244, 120–132.
638 doi:10.1016/j.icarus.2014.03.013
639 Lague, D., Davy, P., 2003. Constraints on the long-term colluvial erosion law by analyzing
640 slope-area relationships at various uplift rates in the Siwaliks Hills (Nepal). J.
641 Geophys. Res. B Solid Earth 108, doi:10.1029/2002JB001893.
642 Lanza, N.L., Meyer, G.A., Okubo, C.H., Newsom, H.E., Wiens, R.C., 2010. Evidence for
643 debris flow gully formation initiated by shallow subsurface water on Mars. Icarus
644 205, 103–112.
645 Lavé, J., Avouac, J.P., 2001. Fluvial incision and tectonic uplift across the Himalayas of
646 central Nepal. J. Geophys. Res. Solid Earth 106, 26561–26591.
647 doi:10.1029/2001JB000359

Levy, J.S., Head, J.W., Dickson, J.L., Fassett, C.I., Morgan, G.A., Schon, S.C., 2010. Identification of gully debris flow deposits in Protonilus Mensae, Mars: Characterization of a water-bearing, energetic gully-forming process. Earth Planet. Sci. Lett., Mars Express after 6 Years in Orbit: Mars Geology from Three-Dimensional Mapping by the High Resolution Stereo Camera (HRSC) Experiment 294, 368–377. doi:10.1016/j.epsl.2009.08.002

Levy, J.S., Head, J.W., Marchant, D.R., 2011. Gullies, polygons and mantles in Martian permafrost environments: cold desert landforms and sedimentary processes during recent Martian geological history. Geol. Soc. Lond. Spec. Publ. 354, 167–182. doi:10.1144/SP354.10

Lewis, S.R., Collins, M., Read, P.L., Forget, F., Hourdin, F., Fournier, R., Hourdin, C., Talagrand, O., Huot, J.P., 1999. A climate database for Mars. J Geophys Res-Planets 104, 24177–24194.

Lindsay, J.B., 2005. The Terrain Analysis System: a tool for hydro-geomorphic applications. Hydrol. Process. 19, 1123–1130. doi:10.1002/hyp.5818

Malin, M.C., Edgett, K.S., 2000. Evidence for recent groundwater seepage and surface runoff on Mars. Science 288, 2330–2335. doi:10.1126/science.288.5475.2330

Mangold, N., Costard, F., Forget, F., 2003. Debris flows over sand dunes on Mars: Evidence for liquid water. J Geophys Res-Planets 108, doi:10.1029/2002JE001958.

Marquez, A., de Pablo, M.A., Oyarzun, R., Viedma, C., 2005. Evidence of gully formation by regional groundwater flow in the Gorgonum-Newton region (Mars). Icarus 179, 398–414.

Massé, M., Conway, S.J., Gargani, J., Patel, M.R., Pasquon, K., McEwen, A.S., Chevrier, V.F., Balme, M.R., 2016. Transport processes resulting from metastable boiling water under Mars surface conditions. Nat. Geosci. 9, 425-428.

McLachlan, G.J., 2004. Discriminant Analysis and Statistical Pattern Recognition. John Wiley & Sons.

McNamara, J.P., Ziegler, A.D., Wood, S.H., Vogler, J.B., 2006. Channel head locations with respect to geomorphologic thresholds derived from a digital elevation model: A case study in northern Thailand. For. Ecol. Manag. 224, 147–156.

Mellon, M.T., Feldman, W.C., Prettyman, T.H., 2004. The presence and stability of ground ice in the southern hemisphere of Mars. Icarus 169, 324–340. doi:doi: 10.1016/j.icarus.2003.10.022

Montgomery, D.R., Foufoula-Georgiou, E., 1993. Channel network source representation using digital elevation models. Water Resour. Res. 29, 3925–3934.

Moore, I.D., Burch, G.J., Mackenzie, D.H., 1988. Topographic effects on the distribution of surface soil water and the location of ephemeral gullies. Trans. Am. Soc. Agric. Eng. 31, 1098–1107.

O'Callaghan, J.F., Mark, D.M., 1984. The extraction of drainage networks from digital elevation data. Comput. Vis. Graph. Image Process. 28, 323–344. doi:10.1016/S0734-189X(84)80011-0

Okubo, C.H., Tornabene, L.L., Lanza, N.L., 2011. Constraints on mechanisms for the growth of gully alcoves in Gasa crater, Mars, from two-dimensional stability assessments of rock slopes. Icarus 211, 207–221.

Pasquon, K., Gargani, J., Massé, M., Conway, S.J., 2016. Present-day formation and seasonal evolution of linear dune gullies on Mars. Icarus 274, 195–210. doi:10.1016/j.icarus.2016.03.024

Perera, H., Willgoose, G., 1998. A physical explanation of the cumulative area distribution curve. Water Resour. Res. 34, 1335–1343.

Pilorget, C., Forget, F., 2016. Formation of gullies on Mars by debris flows triggered by CO2 sublimation. Nat. Geosci 9, 65–69.

Raack, J., Reiss, D., Appéré, T., Vincendon, M., Ruesch, O., Hiesinger, H., 2015. Present-Day Seasonal Gully Activity in a South Polar Pit (Sisyphi Cavi) on Mars. Icarus 251, 226–243. doi:j.icarus.2014.03.040

Reiss, D., Jaumann, R., 2003. Recent debris flows on Mars: Seasonal observations of the Russell Crater dune field. Geophys Res Lett 30, doi:10.1029/2002GL016704.

Reiss, D., van Gasselt, S., Neukum, G., Jaumann, R., 2004. Absolute dune ages and implications for the time of formation of gullies in Nirgal Vallis, Mars. J Geophys Res-Planets 109, doi:10.1029/2004JE002251.

Schon, S.C., Head, J.W., 2011. Keys to gully formation processes on Mars: Relation to climate cycles and sources of meltwater. Icarus 213, 428–432. doi:10.1016/j.icarus.2011.02.020

Schon, S.C., Head, J.W., Fassett, C.I., 2009. Unique chronostratigraphic marker in depositional fan stratigraphy on Mars: Evidence for ca. 1.25 Ma gully activity and surficial meltwater origin. Geology 37, 207–210. doi:10.1130/g25398a.1

Scully, J.E.C., Russell, C.T., Yin, A., Jaumann, R., Carey, E., Castillo-Rogez, J., McSween, H.Y., Raymond, C.A., Reddy, V., Le Corre, L., 2015. Geomorphological evidence for transient water flow on Vesta. Earth Planet. Sci. Lett. 411, 151–163. doi:10.1016/j.epsl.2014.12.004

Senthil Kumar, P., Keerthi, V., Senthil Kumar, A., Mustard, J., Gopala Krishna, B., Amitabh, Ostrach, L.R., Kring, D.A., Kiran Kumar, A.S., Goswami, J.N., 2013. Gullies and landslides on the Moon: Evidence for dry-granular flows. J. Geophys. Res. Planets 118, 206–223. doi:10.1002/jgre.20043

721 Smil, V., 2008. Energy in nature and society: general energetics of complex systems. MIT
722 press.
723 Snyder, N.P., Whipple, K.X., Tucker, G.E., Merritts, D.J., 2000. Landscape response to
724 tectonic forcing: Digital elevation model analysis of stream profiles in the Mendocino
725 triple junction region, Northern California. Bull. Geol. Soc. Am. 112, 1250–1263.
726 Som, S.M., Montgomery, D.R., Greenberg, H.M., 2009. Scaling relations for large Martian
727 valleys. J. Geophys. Res.-Planets 114, doi:10.1029/2008JE003132. doi:E02005
728 10.1029/2008je003132
729 Takahashi, T., 1981. Debris Flow. Annu. Rev. Fluid Mech. 13, 57–77.
730 Takahashi, T., 1978. Mechanical characteristics of debris flow. J. Hydraul. Div. 104, 1153–
731 1169.
732 Tarboton, D.G., 1997. A new method for the determination of flow directions and upslope
733 areas in grid digital elevation models. Water Resour. Res. 33, 309–319.
734 Tesfa, T.K., Tarboton, D.G., Watson, D.W., Schreuders, K.A.T., Baker, M.E., Wallace, R.M.,
735 2011. Extraction of hydrological proximity measures from DEMs using parallel
736 processing. Environ. Model. Softw. 26, 1696–1709.
737 doi:10.1016/j.envsoft.2011.07.018
738 Vincendon, M., 2015. Identification of Mars gully activity types associated with ice
739 composition. J. Geophys. Res. Planets 120, 1859–1879. doi:10.1002/2015JE004909
740 Whipple, K.X., Tucker, G.E., 1999. Dynamics of the stream-power river incision model:
741 Implications for height limits of mountain ranges, landscape response timescales, and
742 research needs. J. Geophys. Res. B Solid Earth 104, 17661–17674.
743 Xiao, Z., Zeng, Z., Ding, N., Molaro, J., 2013. Mass wasting features on the Moon – how
744 active is the lunar surface? Earth Planet. Sci. Lett. 376, 1–11.
745 doi:10.1016/j.epsl.2013.06.015